

See discussions, stats, and author profiles for this publication at: <https://www.researchgate.net/publication/224442436>

# Estimating Spatiotemporal Ground Deformation With Improved Permanent-Scatterer Radar Interferometry

Article in IEEE Transactions on Geoscience and Remote Sensing · September 2009

DOI: 10.1109/TGRS.2009.2016213 · Source: IEEE Xplore

CITATIONS

20

READS

153

5 authors, including:



Sean Buckley

NASA

36 PUBLICATIONS 338 CITATIONS

SEE PROFILE



Xiaoli Ding

The Hong Kong Polytechnic University

296 PUBLICATIONS 3,830 CITATIONS

SEE PROFILE

# Estimating Spatiotemporal Ground Deformation With Improved Persistent-Scatterer Radar Interferometry\*

Guoxiang Liu, Sean M. Buckley, *Member, IEEE*, Xiaoli Ding, Qiang Chen, and Xiaojun Luo

**Abstract**—Synthetic aperture radar interferometry has been applied widely in recent years to ground deformation monitoring although difficulties are often encountered when applying the technology, among which the spatial and temporal decorrelation and atmospheric artifacts are the most prominent. The persistent-scatterer interferometric synthetic aperture radar (PS-InSAR) technique has overcome some of the difficulties by focusing only on the temporally coherent radar targets in a time series of synthetic aperture radar (SAR) images. This paper presents an improved PS-InSAR technique by introducing PS-neighborhood networking and empirical mode decomposition (EMD) approaches in the PS-InSAR solution. Linear deformation rates and topographic errors are estimated based on a least squares method, while the nonlinear deformation and atmospheric signals are computed by singular value decomposition and the EMD method. An area in Phoenix, AZ, is used as a test site to determine its historical subsidence with 39 C-band SAR images acquired by European Remote Sensing 1 and 2 satellites from 1992 to 2000.

**Index Terms**—Atmospheric signal, empirical mode decomposition (EMD), ground deformation, persistent-scatterer (PS) networking, radar interferometry.

## I. INTRODUCTION

REPEAT-PASS satellite differential interferometric synthetic aperture radar (DInSAR) has been proven very useful for regional ground deformation mapping [1]–[4]. However, the quality of DInSAR measurements is highly dependent on the features of the imaged surfaces (such as topography and vegetation coverage) and on the meteorological conditions [5]–[7]. There are two major limitations in applying DInSAR, i.e., spatial and temporal decorrelation [5], [8], [9] and atmospheric artifacts [6], [10], [11]. In general, the longer the time interval between two synthetic aperture radar (SAR)

acquisitions, the lower is the signal-to-noise ratio (SNR) of the interferometric phase due to random surface change over time. This may lead to failure in detecting ground deformation with the DInSAR method particularly in slowly deforming and heavily vegetated areas [7], [12]. The SNR also decreases with the orbital separation of the two SAR acquisitions due to the different radar viewing angles. This effect often reduces the number of usable interferometric pairs. Moreover, spatiotemporal atmospheric inhomogeneity can cause varying phase delays that cannot be canceled out by phase differencing and, therefore, can contaminate deformation measurements.

Efforts have been made in recent years by various researchers to mitigate the aforementioned limitations with DInSAR. For example, the interferogram stacking approach was used to enhance interferometric fringe clarity and suppress atmospheric effects [13], [14]. The persistent-scatterer (PS) InSAR technique was proposed to extract deformation signals from a set of interferograms and to estimate the atmospheric phase screen and digital elevation model (DEM) errors [15], [16]. The PS-InSAR technique models and analyzes PS targets that maintain high SNR in phases [17], [18]. The small-baseline subset (SBAS) approach was subsequently developed to minimize the effects of spatial decorrelation and DEM errors [19], [20].

Unlike the PS-InSAR technique that uses a single master image, the SBAS technique uses all the interferometric combinations within a given spatial baseline threshold, thus often resulting in multiple independent subsets of interferograms. The SBAS technique removes the atmospheric artifacts similarly as in PS technique, and estimates DEM errors and time series of deformations by means of least squares (LS) [21], [22] or singular value decomposition (SVD) [19] technique. In addition, Mora *et al.* [23] extended the PS-InSAR approach by connecting the PS points with the Delaunay triangulation method. The method is a compromise between the PS and SBAS techniques since it detects PS based on coherence instead of amplitude threshold. The number of required images can be reduced with this method, but the spatial resolution of the PS points is limited, and it is impossible to detect certain good PS candidates surrounded by decorrelated pixels [23].

We present in this paper a new PS-InSAR approach for extracting deformation signals from differential interferograms. We propose to connect all PS points within a given threshold of distance, thus forming a so-called freely connected network (FCN). Only interferometric combinations that have both small spatial and temporal baselines are used in the solution. The linear deformation velocities and DEM errors are estimated based on the LS principle and after removing observation outliers [24]. The time series of phase measurements is reconstructed

\*This paper first appeared in the *IEEE Trans. Geosci. Remote Sens.*, vol. 47, no. 8, pt. 2, pp. 2762–2772, Aug. 2009. This version contains corrections that were lost during the production process, most notably a change to the title of the paper.

Manuscript received August 9, 2008; revised January 20, 2009. Current version published August 28, 2009. This work was supported in part by the National Natural Science Foundation of China under Grants 40774004 and 40374003 and in part by the Program for New Century Excellent Talents in University.

G. Liu, Q. Chen, and X. Luo are with the Department of Surveying Engineering, Southwest Jiaotong University, Chengdu 610031, China (e-mail: rsgxliu@swjtu.edu.cn; qchen@swjtu.edu.cn; lxj@swjtu.edu.cn).

S. M. Buckley is with the Department of Aerospace Engineering and Engineering Mechanics, The University of Texas at Austin, Austin, TX 78712-1085 USA (e-mail: sean.buckley@mail.utexas.edu).

X. Ding is with the Department of Land Surveying and Geo-Informatics, The Hong Kong Polytechnic University, Kowloon, Hong Kong (e-mail: lsxlding@polyu.edu.hk).

Color versions of one or more of the figures in this paper are available online at <http://ieeexplore.ieee.org>.

Digital Object Identifier 10.1109/TGRS.2009.2028797

by SVD as done in the SBAS technique and then decomposed into nonlinear deformations and atmospheric signals by using the empirical mode decomposition (EMD) [25]. The obvious feature of our approach is that the PS solutions are based on the use of FCN and EMD which help improve the extraction and the separation of signals of interest.

## II. PS DETECTION AND PHASE MODELING

Suppose that  $M$  differential interferograms have been generated from a set of  $N + 1$  SAR images (ordered by the time of SAR acquisitions,  $t_0, t_1, \dots, t_N$ ) over a study area. Any interferometric combinations can be used as long as their temporal and spatial baselines are within given thresholds. Experiences (e.g., [9]) have indicated that it is reasonable to set the temporal- and spatial-baseline thresholds as four years and 120 m, respectively. The spatial baseline should be much smaller than the critical baseline [e.g., about 1100 m for the European Remote Sensing (ERS) satellite case]. When coregistering the images, a SAR image roughly in the middle of the time series should be used as the reference image to minimize the temporal effects in imaging matching.

The method used for PS detection basically follows that proposed by Ferretti *et al.* [16]. We, however, first carry out radiometric calibration for all the amplitude images similarly to Lyons and Sandwell [14]. A radiometric calibration factor is calculated for each image as the ratio between the amplitude of the image (mean of all pixels) to the mean amplitude of all the images. Each SAR amplitude image is then divided by this ratio to make the brightness between the images consistent and comparable. The calibrated images are then averaged to generate a multi-image reflectivity map. The mean amplitude and the standard deviation (SD) of each pixel, and the overall mean amplitude and SD of all the pixels can be calculated based on the calibrated amplitude images. A pixel is considered as a PS candidate only if it satisfies the following two empirical criteria simultaneously:

$$\begin{cases} D_a = \frac{\sigma_a}{\bar{a}} \leq 0.25 \\ \bar{a} \geq \bar{A} + 2\sigma_A \end{cases} \quad (1)$$

where  $D_a$  is the amplitude dispersion index [16]. Pixels with high amplitude values tend to be temporally more coherent. The PS candidates will be assessed again based on the phase data as discussed in the next section.

The phase value of a pixel with coordinates  $(x, y)$  extracted from the  $i$ th differential interferogram can be modeled as

$$\Phi_i(x, y; T_i) = \frac{4\pi}{\lambda \cdot R \cdot \sin \theta} \cdot B_i^\perp \cdot \varepsilon(x, y) + \frac{4\pi}{\lambda} \cdot T_i \cdot v(x, y) + \phi_i^{\text{res}}(x, y; T_i) \quad (2)$$

where

- 1)  $B_i^\perp$  and  $T_i$  are the perpendicular (spatial) and temporal baseline, respectively;
- 2)  $\lambda$ ,  $R$ , and  $\theta$  are the radar wavelength (5.66 cm for ERS case), sensor-to-target distance, and radar incident angle, respectively;

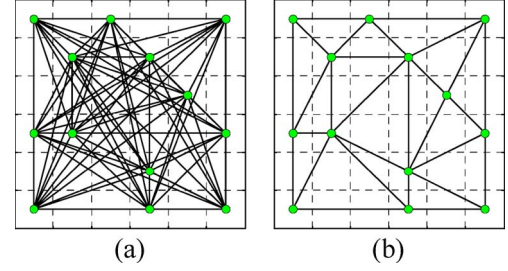


Fig. 1. Examples of PS networking. (a) FCN [9]. (b) TIN.

- 3)  $\varepsilon(x, y)$ ,  $v(x, y)$ , and  $\phi_i^{\text{res}}(x, y; T_i)$  are the elevation error, linear deformation velocity along radar line of sight (LOS), and residual phase, respectively.

$\Phi_i(x, y; T_i)$  in (2) is a wrapped phase value in the principal interval of  $[-\pi, \pi)$ . Moreover, the residual phase  $\phi_i^{\text{res}}(x, y; T_i)$  can be expressed as a sum of three contributions, including nonlinear deformation ( $\phi_i^{\text{nldf}}$ ), atmospheric effect ( $\phi_i^{\text{atm}}$ ), and decorrelation noise ( $\phi_i^{\text{noi}}$ ), i.e.,

$$\phi_i^{\text{res}}(x, y; T_i) = \phi_i^{\text{nldf}}(x, y; T_i) + \phi_i^{\text{atm}}(x, y; T_i) + \phi_i^{\text{noi}}(x, y; T_i). \quad (3)$$

## III. PS NEIGHBORHOOD NETWORKING AND LINEAR DEFORMATION ESTIMATION

### A. PS Network Formation

We propose to link all the neighboring PS points that fall within a given threshold of Euclidian distance, instead of using the Delaunay triangulation method commonly used in PS solutions [17], [23]. Any two PS points ( $l$  and  $p$ ) will be connected if the following criterion is met:

$$S(x_l, y_l; x_p, y_p) = \sqrt{f_r^2 \cdot (x_p - x_l)^2 + f_a^2 \cdot (y_p - y_l)^2} \leq S_0 \quad (4)$$

where

- 1)  $x$  and  $y$  are pixel coordinates in the image space;
- 2)  $f_r$  and  $f_a$  are scaling factors (converting pixel dimensions into geometric distances) in range and azimuth directions, respectively (e.g.,  $f_r \approx 22$  m,  $f_a \approx 4$  m for the case of the ERS SAR system);
- 3)  $S_0$  is the distance threshold.

$S_0$  is chosen by considering mainly the atmospheric gradients in the space domain. The faster the atmospheric delay varies spatially, the shorter the distance threshold should be. As an example, Fig. 1(a) shows a network constructed using (4), herein termed FCN, while Fig. 1(b) shows a triangular irregular network (TIN) constructed from the same PS points according to the principle of Delaunay triangulation. It can be seen that the FCN has much more connections than the TIN. The advantages of the FCN will be discussed further in Section V.

### B. Network Modeling and Parameter Estimation

We will extend the mathematical models required for understanding PS solution in this and the next subsections, although

some preliminary results have been described in [9]. In Global Positioning System (GPS) data processing, the concept of differencing is commonly employed to mitigate correlating errors (e.g., atmospheric effects) in GPS carrier-phase measurements [24]. Similar concept can be used in analyzing PS networks to improve the quality of the solutions. According to (2), the differential phase between two adjacent PS points ( $l$  and  $p$ ) from the  $i$ th differential interferogram can be expressed as

$$\Delta\Phi_i(x_l, y_l; x_p, y_p; T_i) = \frac{4\pi}{\lambda \cdot \bar{R} \cdot \sin \bar{\theta}} \cdot \bar{B}_i^\perp \cdot \Delta\varepsilon(x_l, y_l; x_p, y_p) + \frac{4\pi}{\lambda} \cdot T_i \cdot \Delta v(x_l, y_l; x_p, y_p) + \Delta\phi_i^{\text{res}}(x_l, y_l; x_p, y_p; T_i) \quad (5)$$

where  $\bar{B}_i^\perp$ ,  $\bar{R}$ , and  $\bar{\theta}$  are the mean perpendicular baseline, the mean sensor-to-target distance, and the mean incident angle of the two PS points, respectively;  $\Delta\varepsilon$  and  $\Delta v$  are the differential elevation error and the differential linear deformation velocity, respectively, between the two points, and can be written as

$$\Delta\varepsilon(x_l, y_l; x_p, y_p) = \varepsilon(x_p, y_p) - \varepsilon(x_l, y_l) \quad (6)$$

$$\Delta v(x_l, y_l; x_p, y_p) = v(x_p, y_p) - v(x_l, y_l). \quad (7)$$

Similarly, the differential residual phase between the two PS points can be expressed as

$$\Delta\phi_i^{\text{res}}(x_l, y_l; x_p, y_p; T_i) = \Delta\phi_i^{\text{nldf}}(x_l, y_l; x_p, y_p; T_i) + \Delta\phi_i^{\text{atm}}(x_l, y_l; x_p, y_p; T_i) + \Delta\phi_i^{\text{noi}}(x_l, y_l; x_p, y_p; T_i) \quad (8)$$

where  $\Delta\phi_i^{\text{nldf}}$ ,  $\Delta\phi_i^{\text{atm}}$ , and  $\Delta\phi_i^{\text{noi}}$  are the differential phases for nonlinear deformation, atmospheric delay, and decorrelation noise, respectively

$$\Delta\phi_i^{\text{nldf}}(x_l, y_l; x_p, y_p; T_i) = \phi_i^{\text{nldf}}(x_p, y_p; T_i) - \phi_i^{\text{nldf}}(x_l, y_l; T_i) \quad (9)$$

$$\Delta\phi_i^{\text{atm}}(x_l, y_l; x_p, y_p; T_i) = \phi_i^{\text{atm}}(x_p, y_p; T_i) - \phi_i^{\text{atm}}(x_l, y_l; T_i) \quad (10)$$

$$\Delta\phi_i^{\text{noi}}(x_l, y_l; x_p, y_p; T_i) = \phi_i^{\text{noi}}(x_p, y_p; T_i) - \phi_i^{\text{noi}}(x_l, y_l; T_i). \quad (11)$$

Due to spatial autocorrelation, the atmospheric contributions, the nonlinear deformations and the orbital errors can be largely canceled out with the differencing operation as denoted by (5)–(11). This facilitates the estimation of the linear terms ( $\Delta\varepsilon$  and  $\Delta v$ ) that are constant in all the differential interferograms.

Ferretti *et al.* [15], [16] indicated that if  $\Delta\phi_i^{\text{res}}$  is small enough, for example,  $|\Delta\phi_i^{\text{res}}| < \pi$ , it is possible to estimate both  $\Delta\varepsilon$  and  $\Delta v$  directly from the  $M$  wrapped differential interferograms by maximizing the following objective function:

$$\gamma = \left| \frac{1}{M} \sum_{i=1}^M (\cos \Delta\omega_i + j \cdot \sin \Delta\omega_i) \right| = \text{maximum} \quad (12)$$

where  $\gamma$  is called model coherence (MC) of the two PS points;  $j = \sqrt{-1}$ ; and  $\Delta\omega_i$  denotes the difference between the mea-

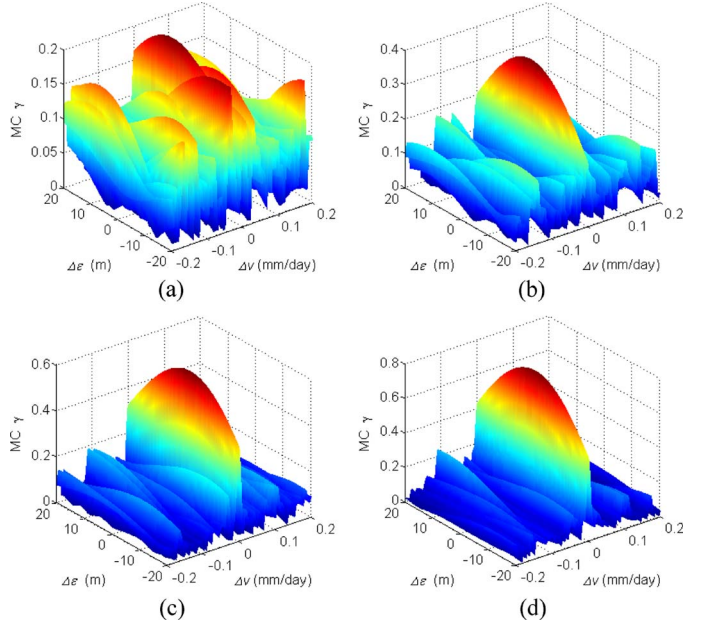


Fig. 2. MC surface is represented as a function of  $\Delta\varepsilon$  and  $\Delta v$ . (a)–(d) show examples of typical MC surfaces with peak coherence values  $\gamma_{\text{max}} = 0.2, 0.4, 0.6$ , and  $0.8$ , respectively. (a)  $\gamma_{\text{max}} = 0.2$ . (b)  $\gamma_{\text{max}} = 0.4$ . (c)  $\gamma_{\text{max}} = 0.6$ . (d)  $\gamma_{\text{max}} = 0.8$ .

sured and the estimated phase values, i.e.,

$$\Delta\omega_i = \Delta\phi_i - \frac{4\pi}{\lambda \cdot \bar{R} \cdot \sin \bar{\theta}} \cdot \bar{B}_i^\perp \cdot \Delta\varepsilon - \frac{4\pi}{\lambda} \cdot T_i \cdot \Delta v. \quad (13)$$

Although the objective function is highly nonlinear and the measured phase values are wrapped, the two unknowns  $\Delta\varepsilon$  and  $\Delta v$  corresponding to each pair of PS points can be determined by searching within a predefined solution space (constraint) to maximize the MC value. Phase unwrapping can be avoided through the process of function optimization, although this is sometimes difficult for the case of sparse PS points.

Simulation studies have been carried out to examine how  $\gamma$  varies within a given solution space. Fig. 2 shows typical examples of MC surfaces corresponding to four pairs of PS points with their peak coherence values  $\gamma_{\text{max}} = 0.2, 0.4, 0.6$ , and  $0.8$ , respectively. Each of surfaces is represented as a 2-D function of  $\Delta\varepsilon$  and  $\Delta v$ . The maximal value of each MC surface corresponds to the final solution of  $\Delta\varepsilon$  and  $\Delta v$ . It should be noted that the spectral features are different between the two search dimensions. The frequency in the direction of  $\Delta v$  is much higher, and the variation is more complicated than those in the direction of  $\Delta\varepsilon$ . This indicates that the system is more sensitive to deformations than DEM errors, due to the short interferometric baselines selected. This means that the estimation of deformations is more reliable than that of DEM errors. In addition, if we define here the kurtosis of an MC surface as the difference between  $\gamma_{\text{max}}$  and the overall mean of the MC values, it is proportional to  $\gamma_{\text{max}}$  and highly dependent on the degrees of decorrelation at the two PS points. This indicates that  $\gamma_{\text{max}}$  can be used as a quality measure for the differential interferometric phases of a pair of PS points.

Fig. 3 shows the kurtosis as a function of different peak coherence values, as obtained from statistical analysis of 50 000

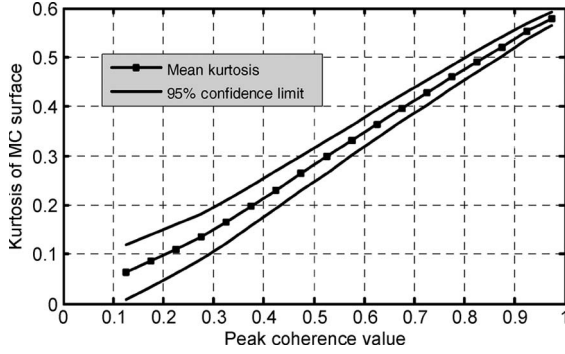


Fig. 3. Kurtosis of MC surface goes up almost linearly with the increase in peak coherence value.

pairs of PS points from simulated data. The kurtosis goes up almost linearly with the increase in  $\gamma_{\max}$ , while its 95% confidence limit becomes narrower and narrower. The results show that the differential interferometric phases corresponding to a pair of PS points can be most likely regarded as being of good quality if its peak coherence value is above 0.45, although a threshold value of  $> 0.70$  has been used in the previous studies [15], [16], [23].

### C. Network Adjustment

The increments of elevation errors and linear deformation velocities along all the connected PS pairs in a PS network can be computed with (12) and (13). The PS network must be first “cleaned up” by deleting the connections with their MC below 0.45 and the isolated PS candidates. The incremental values derived from the reduced PS network can be treated as observations similarly to those in a leveling or GPS network [24]. LS adjustment computation can be performed to eliminate the geometric inconsistencies (i.e., misclosures of loops) and obtain the most probable estimates of the linear deformation rates and elevation errors at all the PS points. The two types of values: linear deformation rates and elevation errors can be estimated separately. For example, the observation equation for the linear deformation rate increment between two PS points is

$$\hat{v}_p - \hat{v}_l = \Delta v_{pl} + r_{pl}, \quad p \neq l, \quad \forall p, \quad l = 1, 2, \dots, T \quad (14)$$

where  $\hat{v}_l$  and  $\hat{v}_p$  are the linear deformation rates of the two PS points ( $l$  and  $p$ );  $\Delta v_{pl}$  is the linear deformation rate increment between the two points;  $r_{pl}$  is the residual of  $\Delta v_{pl}$ ;  $T$  is the number of PS points in the network. The matrix form of the observation equations is

$$\mathbf{B} \cdot \mathbf{X} = \mathbf{L} + \mathbf{R} \quad (15)$$

$Q \times T \quad T \times 1 \quad Q \times 1 \quad Q \times 1$

where  $\mathbf{B}$  is a coefficient matrix that is highly sparse and has nonzero elements of either 1 or  $-1$ ;  $\mathbf{L}$  and  $\mathbf{R}$  are the vectors of the observations (linear deformation rate increments) and the residuals, respectively;  $Q$  is the number of connections in the network;  $\mathbf{X}$  is the vector of unknown linear deformation rates to be estimated, i.e.,

$$\mathbf{X} = [\hat{v}_1, \hat{v}_2, \dots, \hat{v}_T]^T. \quad (16)$$

Furthermore, let the weight matrix be

$$\mathbf{P} = \begin{bmatrix} \gamma_1^2 & 0 & 0 & 0 \\ 0 & \gamma_2^2 & 0 & 0 \\ \vdots & \vdots & \vdots & \vdots \\ 0 & 0 & 0 & \gamma_Q^2 \end{bmatrix} \quad (17)$$

whose diagonal elements are the squares of the MC values previously estimated for the PS pairs. Therefore, the LS solution of the unknowns  $\mathbf{X}$  can be expressed as

$$\mathbf{X} = (\mathbf{B}^T \mathbf{P} \mathbf{B})^{-1} \mathbf{B}^T \mathbf{P} \mathbf{L}. \quad (18)$$

A reference point (e.g., a point located in a stable area) needs to be chosen and used in the solution. The deformation rates of all the other PS points are estimated relatively to this reference point. The large sparse linear system is solved with an algorithm based on the unsymmetric multifrontal method and direct sparse LU factorization [26].

After the LS solutions, the standardized residuals, i.e., the ratios between the LS residuals and their SDs, corresponding to all the connections are computed. Outlying observations are identified by comparing the standardized residuals with a threshold value determined based on a function of Type I and Type II errors  $\partial_0$  and  $\beta_0$  [24]. In our analysis, a threshold value of 4.13 is used based on  $\partial_0 = 0.1\%$  and  $\beta_0 = 80\%$ .

Any connection that is detected as an outlier is removed from the network. Isolated PS points resulted from the removal of the outlying connections are also removed from the network. The LS adjustment computations are repeated with the new (cleaned) data sets. The process continues until all the hypothesis tests can pass. From the standpoint of reliability, the FCN, as shown in Fig. 1(a) is much stronger for outlier detection than the TIN, as shown in Fig. 1(b).

## IV. SIGNAL DECOMPOSITION AND NONLINEAR DEFORMATION ESTIMATION

Once the LOS linear deformation rate  $\hat{v}$  and the DEM error  $\hat{\varepsilon}$  at each of the PS points are estimated as discussed above, further analysis needs carried out to isolate the nonlinear deformations from the atmospheric artifacts. Linear deformation rates and DEM errors at the regular grid points of the original interferograms are first generated by using the Kriging interpolator [27] based on the irregular samples at the PS points. Subtracting the linear terms from each of the differential interferograms results in the residual phases

$$\begin{aligned} \phi_i^{\text{res}}(x, y; T_i) &= \Phi_i(x, y; T_i) - \frac{4\pi}{\lambda \cdot R \cdot \sin \theta} \\ &\quad \times B_i^\perp \cdot \hat{\varepsilon}(x, y) - \frac{4\pi}{\lambda} \cdot T_i \cdot \hat{v}(x, y) \end{aligned} \quad (19)$$

where subscript  $i$  refers to the  $i$ th interferogram. The residual differential interferograms possibly consist of three components, i.e., nonlinear deformations, atmospheric delays, and decorrelation noises as described by (3).

It is possible to separate the nonlinear deformations from the atmospheric phases based on the  $M$  residual differential



interferograms as the two terms have in general different frequency structures in space and time [15], [19], [20], [23]. The atmospheric perturbations exhibit typically high spatial correlation but low temporal correlation. Previous studies have indicated that the correlation distance of atmospheric phases is mainly within about 1 km [6], [28]. On the other hand, nonlinear deformations have in general a shorter spatial correlation distance and low temporal frequency. It is however not easy to discriminate between the spectral bands of the nonlinear deformations and the atmospheric phases in the case that no *a priori* information is available. We attempt to discriminate between the signals by using EMD proposed by Huang *et al.* [25]. The method is in principle different from the cascade filter applied in the previous studies [15], [16], [23].

Prior to applying EMD, the residual differential interferograms are first filtered to suppress the decorrelation noise using, e.g., Goldstein and Werner [29] and Li *et al.* [30], and then unwrapped to obtain the residual phases in absolute sense. The path-following integration method [31] is used for the phase unwrapping which can be easily performed as the fringe rates in the residual interferograms have been significantly reduced after removing the linear terms. As the interferometric combinations are freely generated, the SVD is finally used to reconstruct the time series of residual phases corresponding to the  $N + 1$  SAR acquisitions (for details see [19]).

The time series of residual phases thus obtained have in general several features. First, there are typically several tens of irregular samples. Second, the data series are nonstationary. Finally, the data series represent nonlinear processes. The EMD approach is usually more advantageous for dealing with nonlinear and nonstationary processes than the other signal analysis tools like Fourier transform [25]. The  $N + 1$  residual phases at any pixel corresponding to the time of SAR acquisitions ( $t_0, t_1, \dots, t_N$ ) can be expressed as

$$\psi(t) = [\psi(t_0), \psi(t_1), \dots, \psi(t_N)]. \quad (20)$$

The procedures of applying the EMD technique are as follows.

- 1) Identify all extrema of the input data  $\psi(t)$ .
- 2) The local maxima are connected by a cubic spline curve to obtain the upper envelope  $e_{\max}(t)$ . Repeat this for the local minima to yield the lower envelope  $e_{\min}(t)$ .
- 3) Compute the mean  $m(t) = (e_{\min} + e_{\max})/2$ .
- 4) Get the detail  $d(t) = \psi(t) - m(t)$ .
- 5) Replace the input with  $d(t)$  and repeat steps 1)–4) until attaining the predefined stop criterion. The ultimate  $d(t)$  can be considered as a true intrinsic mode function (IMF).
- 6) Get the residual  $h(t) = \psi(t) - d(t)$ , replace the input with  $h(t)$ , and repeat steps 1)–5) to extract other IMFs.

In practice, steps 1)–4) must be iterated several times in order to obtain each level of a true IMF. Such iteration is usually referred to as a sifting process which aims to eliminate riding waves and make the wave-profiles more symmetric. The sifting is terminated when the relative SD computed from the difference of two consecutive details  $d_{k-1}(t)$  and  $d_k(t)$  is less than a given threshold (typically set between 0.2 and 0.3) [25]. All these guarantee that each IMF has a zero mean and the

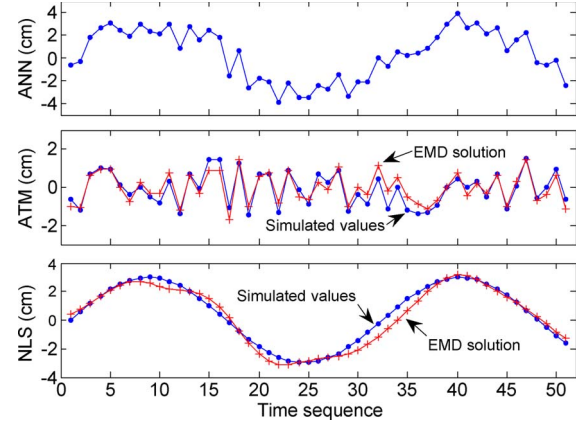


Fig. 4. Simulated data set (combined ATM delays, NLS and random noises, top panel) and the extracted ATM and NLS with the EMD technique (middle and bottom panels, respectively).

number of extrema and the number of zero crossings are equal or differ at most by one. Moreover, the number of extrema is reduced when going from one level of the residual to the next, and the whole decomposition can be completed with a finite number of IMFs [32].

A simulation experiment has been carried out to examine and to validate the capability of EMD in separating nonlinear deformation signals from atmospheric delays. Time series of nonlinear subsidence values (NLS), atmospheric (ATM) delays and random noises are first simulated. The NLS values are generated with the formula  $3 \cdot \sin(0.2 \cdot t)$  (in cm,  $t = 1, 2, \dots, 51$ ). The ATM delays are created with a random number generator with a uniform distribution over the interval of  $(-1.5 \text{ cm}, 1.5 \text{ cm})$ . The random noises follow a normal distribution with zero mean and an SD of 2.5 mm. The sum (ANN) of the three time series is shown in top panel of Fig. 4. The EMD technique is then applied to extract the simulated signals from the combined data series and the results are shown in the mid and bottom panels of Fig. 4. The root mean square (rms) values of the differences between the extracted and the true ATM and NLS values are 3.7 and 3.8 mm, respectively. The experiment has demonstrated that the EMD technique is capable of separating the nonlinear deformations from the atmospheric effects in this case.

Extensive experiments with SAR data have shown that four IMFs can be extracted typically from a time series of phase residuals. The IMFs with high frequencies correspond more likely to the atmospheric components, while those with low frequencies reflect nonlinear deformations. Although it is not very obvious to discriminate exactly between the signals in the case that no *a priori* information is available, very reasonable results have been obtained in our tests when the sums of the first and second levels of IMFs are considered as the atmospheric phases and those of the third and fourth levels of IMFs are considered as nonlinear deformations. The two decomposed terms can be expressed as

$$\psi^{\text{nldf}}(t) = [\psi^{\text{nldf}}(t_0), \psi^{\text{nldf}}(t_1), \dots, \psi^{\text{nldf}}(t_N)] \quad (21)$$

$$\psi^{\text{atm}}(t) = [\psi^{\text{atm}}(t_0), \psi^{\text{atm}}(t_1), \dots, \psi^{\text{atm}}(t_N)]. \quad (22)$$

TABLE I  
EIGHTY-SIX SHORT BASELINE INTERFEROGRAMS FORMED

| Master/Slave<br>Dates, YMD <sup>a</sup> | $B^\perp$<br>(m) | $T$<br>(days) | Master/Slave<br>Dates, YMD | $B^\perp$<br>(m) | $T$<br>(days) | Master/Slave<br>Dates, YMD | $B^\perp$<br>(m) | $T$<br>(days) |
|---|------------------|---------------|----------------------------|------------------|---------------|----------------------------|------------------|---------------|
| 920710/930521                           | 24               | 315           | 950827/960916              | 104              | 386           | 961230/970519              | -35              | 140           |
| 920710/931008                           | -78              | 455           | 950827/980330              | 52               | 946           | 961230/981130              | -86              | 700           |
| 920710/950827                           | -85              | 1143          | 950827/981130              | 88               | 1191          | 961230/990802              | -65              | 945           |
| 920814/930205                           | -25              | 175           | 950827/990802              | 109              | 1436          | 961230/991220              | -21              | 1085          |
| 920814/950514                           | 80               | 1003          | 951105/951210              | -68              | 35            | 961230/001030              | 54               | 1400          |
| 920814/960603                           | 36               | 1389          | 951105/961021              | 106              | 351           | 970310/970519              | -91              | 70            |
| 920918/951106                           | -79              | 1144          | 951106/951211              | -51              | 35            | 970310/990315              | 73               | 735           |
| 920918/951210                           | 64               | 1178          | 951106/980504              | 16               | 910           | 970310/991220              | -76              | 1015          |
| 921023/960812                           | 113              | 1389          | 951106/990628              | -65              | 1330          | 970310/001030              | -2               | 1330          |
| 930205/950514                           | 105              | 828           | 951211/980504              | 67               | 875           | 970519/980330              | -88              | 315           |
| 930205/960603                           | 60               | 1214          | 951211/990628              | -15              | 1295          | 970519/981130              | -51              | 560           |
| 930521/931008                           | -101             | 140           | 960218/960219              | 53               | 1             | 970519/990802              | -31              | 805           |
| 930521/950827                           | -109             | 828           | 960218/961021              | -35              | 246           | 970519/991220              | 14               | 945           |
| 930521/960916                           | -5               | 1214          | 960218/980608              | -5               | 841           | 970519/001030              | 89               | 1260          |
| 930521/961230                           | 65               | 1319          | 960219/960428              | 87               | 69            | 980223/980713              | 90               | 140           |
| 930521/970519                           | 31               | 1459          | 960219/961021              | -88              | 245           | 980330/981130              | 37               | 245           |
| 930903/961230                           | -98              | 1214          | 960219/980608              | -58              | 840           | 980330/990802              | 57               | 490           |
| 930903/970310                           | -42              | 1284          | 960603/980223              | 31               | 630           | 980330/991220              | 103              | 630           |
| 931008/950827                           | -8               | 688           | 960812/971215              | -112             | 490           | 980504/990628              | -81              | 420           |
| 931008/960812                           | -41              | 1039          | 960812/980330              | 85               | 595           | 980608/000508              | 13               | 700           |
| 931008/960916                           | 97               | 1074          | 960916/961230              | 70               | 105           | 981130/990802              | 21               | 245           |
| 931217/960218                           | -73              | 793           | 960916/970519              | 36               | 245           | 981130/991220              | 65               | 385           |
| 931217/960219                           | -19              | 794           | 960916/980330              | -52              | 560           | 990315/990524              | 50               | 70            |
| 931217/960428                           | 68               | 863           | 960916/981130              | -16              | 805           | 990315/001030              | -75              | 595           |
| 931217/961021                           | -107             | 1039          | 960916/990802              | 5                | 1050          | 990524/990628              | 110              | 35            |
| 950514/960603                           | -44              | 386           | 960916/991220              | 50               | 1190          | 990802/991220              | 46               | 140           |
| 950514/980223                           | -13              | 1016          | 961021/980608              | 29               | 595           | 990802/001030              | 119              | 455           |
| 950514/980713                           | 76               | 1156          | 961021/000508              | 42               | 1295          | 991220/001030              | 75               | 315           |
| 950827/960812                           | -33              | 351           | 961230/970310              | 56               | 70            |                            |                  |               |

<sup>a</sup>YMD: year, month, day; Read 920710 as July 10, 1992, and 001030 as October 30, 2000.

The overall deformation at a pixel  $(x, y)$  can be computed by summing the linear and nonlinear components, i.e.,

$$def(x, y; t_i) = (t_i - t_0) \cdot \hat{v}(x, y) + \frac{\lambda}{4\pi} \cdot \psi^{nldef}(x, y; t_i). \quad (23)$$

## V. EXPERIMENTAL DATA SETS AND RESULTS

ERS SAR images over western Phoenix, AZ, are used to study the spatiotemporal subsidence distribution in the area. Large amount of groundwater is stored in the permeable alluvium of the valleys in the area. However, excessive groundwater withdrawal for agricultural, industrial, and urban developments has resulted in uneven ground subsidence across the area. Early interferometric studies with limited sets of ERS SAR images have indicated that several subsiding bowls existed in the town areas [8], [33].

### A. Interferometric Data Sets

Thirty-nine ERS SAR images acquired during 1992–2000 over the area are used to form 86 interferograms with spatial

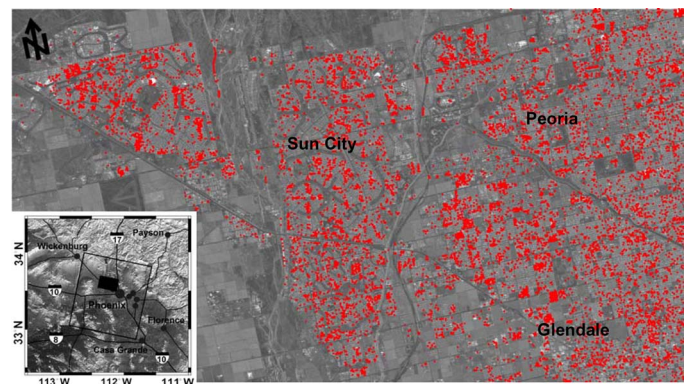


Fig. 5. SAR amplitude image of study area averaged from all the images. The PS candidates in red are superimposed, and the three towns are annotated. The inset shows the geographical setting of (tilted dark box) the study area in the Phoenix metropolitan area. The tilted rectangle identifies the SAR scene.

and temporal baselines smaller than 120 m and four years, respectively, as shown in Table I. We concentrate on a patch of 27 km by 15 km within the SAR scene. Fig. 5 shows the SAR

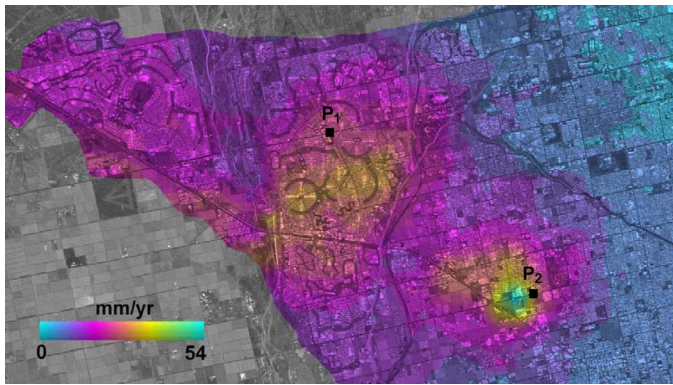


Fig. 6. Map of linear subsidence rates in millimeters per year, superimposed onto the averaged SAR amplitude image. The subsidence in the farmland cannot be estimated due to the lack of PS points in the area. P1 and P2 are two PS points to be analyzed in Fig. 9.

amplitude image of the area averaged from all the images. Most of the area is urban suburbs with the major streets appearing as dark lines and buildings bright spots, while a small part of the area is farmland located in the lower left corner. The detected PS candidates (to be discussed later) that are basically within the urban area are superimposed onto the amplitude image.

Differential interferograms are generated with the “two-pass” method [1] by using Gamma DIFF software. Precise orbit state vectors computed by the Delft University of Technology and the Shuttle Radar Topography Mission (SRTM) DEM data with height accuracy of about 10 m are used to remove the flat-earth trend and the topographic components. Both the SAR images and the differential interferograms have been processed with a multilooking factor of five in azimuth and one in range, resulting in pixel dimension of about 20 m by 20 m.

### B. Experimental Results

As shown in Fig. 5, 14 618 temporal-coherent PS candidates are selected by applying the criteria given in (1). As expected, the density of the PS points appears high in the urban areas, 48/km<sup>2</sup> on average, while that in the farmland is very low. A very strong network of PS points is formed by freely connecting the PS to all those that are within 1 km in distance [see (4)], resulting in 1 463 306 connected PS pairs in total. The increments of both linear deformation rates and elevation errors along each of the pairs are then estimated by maximizing the MC with (12) and (13). An MC threshold of 0.45 is used to reject pairs with low MC and nonconnected PS candidates. As a result, 14 493 PS pixels and 1 433 233 connected PS pairs remain as the input for the subsequent LS network adjustment computation and outlier detection. The linear deformation rates and DEM errors at 14 428 PS points are eventually estimated from 1 225 265 “clean” PS pairs.

Fig. 6 shows the linear subsidence rate (in millimeters per year) map derived after Kriging interpolation and by projecting the LOS displacements to vertical direction. It can be seen that a subsiding bowl with a diameter of about 5 km appears in Glendale that has a peak subsidence rate of 54 mm/yr, while a wider subsiding bowl with a diameter of about 15 km spans Glendale, Peoria, and Sun City and has a peak subsidence

rate of 30 mm/yr. It can be inferred from the results that the accumulative linear subsidence over the time period of the SAR acquisitions (about eight years) is up to 43 and 24 cm, respectively, at the two peak points. The eastern part of the study area appears basically stable. In the farmland to the northwest of Sun City (see Fig. 5), the linear subsidence rates derived with the Kriging interpolator may be less reliable due to the sparsity of the PS points in the area.

Since there are no ground truth data available to validate the results, we check the results against some of those obtained from differential interferograms. Four independent differential interferograms covering different time intervals (one–four years) are shown in Fig. 7 along with the corresponding interferograms simulated based on the linear subsidence rates estimated. It is evident that the simulated and the observed interferograms agree well in general with each other. The minor discrepancies in some of the areas may be due to atmospheric artifacts, topographic errors and nonlinear deformations. The discrepancies in the results obtained from data of June to September [see Fig. 7(f) and (h)] are more apparent perhaps because this is the monsoon season in Phoenix so that the high temperature and varying humidity resulted in more significant atmospheric turbulence [8]. Comparatively, the subsidence variations can be more easily identified with the simulated interferograms. The results not only verify that the proposed approach is powerful and reliable, but also suggest that the linear subsidence in the study area is dominant.

We have also carried out the solution using a TIN formed by linking PS pixels with Delaunay triangles and deleting PS pairs larger than 1 km apart. For comparison, Table II lists the statistical results on the reliability values (minimum redundancy numbers, a measure of network reliability, e.g., [34] and [35]), the number of connected PS pairs and PS pixels remaining at the several estimation stages in the case of FCN and TIN, respectively. The number of connected PS pairs in the FCN is over 30 times more than that in the TIN in all the stages. The minimum redundancy number for the FCN is 0.96, significantly larger than that (0.45) for the TIN, indicating that it is much easier to detect outliers in the FCN. More importantly, more PS candidates are removed from the TIN when carrying out MC thresholding and outlier detecting as the weak TIN results in more isolated PS points. Therefore, at the end, only 12 550 valid PS points remain in the TIN compared to 14 428 in the FCN. As the computer time of a PS solution is primarily governed by the numbers of  $\Delta\epsilon$  and  $\Delta v$  to be estimated with (12), the computer time of the FCN-based PS solutions can be potentially much higher than that of the TIN-based PS solutions as there are usually much more PS connections in an FCN than in a TIN. For example, for the study area, the computer time of the FCN-based PS solutions is about 30 times more than that of the TIN-based PS solutions.

Fig. 8 shows the PS points around Glendale (see Fig. 5) and their subsidence rates (in millimeters per year) derived with the TIN and the FCN methods, respectively. Points that remain in the FCN but not in the TIN are identified in some of the areas with arrows. The subsidence rates from the TIN method appear to be underestimated particularly around the center of the deep subsidence bowl in Glendale.



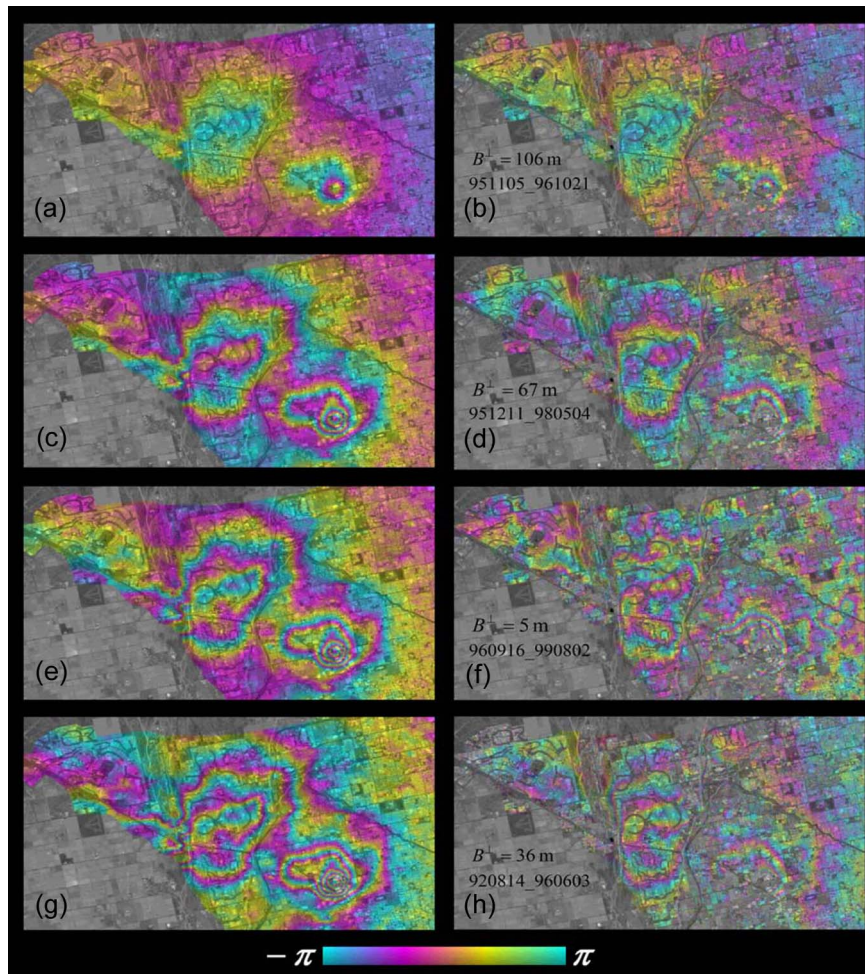


Fig. 7. Comparison between (left) the simulated and (right) the observed independent interferograms. Cases corresponding to four different time intervals are given. (a), (b) November 5, 1995–October 21, 1996. (c), (d) December 11, 1995–May 4, 1998. (e), (f) September 16, 1996–August 2, 1999. (g), (h) August 14, 1992–June 3, 1996.

TABLE II  
COMPARISON BETWEEN TWO TYPES OF PS NETWORK

|   | FCN     | TIN   |
|---|---------|-------|
| Initial total of PS candidates                | 14618   | 14618 |
| Initial total of PS connections               | 1463306 | 43561 |
| Total of PS points after MC thresholding      | 14493   | 13663 |
| Total of PS connections after MC thresholding | 1433233 | 40030 |
| Total of PS points after LS adjustment        | 14428   | 12550 |
| Total of PS connections after LS adjustment   | 1225265 | 38030 |
| Minimum redundancy number                     | 0.96    | 0.45  |

Once the linear subsidence rates have been determined, estimation of the nonlinear subsidence is then carried out with the SVD and EMD algorithms. As examples, Fig. 9 shows the temporal evolution of the atmospheric delays in the LOS direction, the nonlinear and total subsidence values at two PS points (P1 and P2) near the centers of the two subsidence bowls (see Fig. 6). The atmospheric artifacts vary quite randomly from about  $-2.0$  to  $2.0$  cm. The nonlinear subsidence of P1 ranges from  $-2.0$  to  $1.4$  cm while that of P2 from  $-2.5$  to  $2.2$  cm.

In addition, it can be seen that that P2 exhibits more seasonal subsidence than P1, and that the linear trends of subsidence dominate at both of the two points.

Although the problems with long spatial baselines have been studied previously (e.g., [19], [20], and [23]), the effects of long temporal baselines have been rarely discussed in detail. We have performed a test to examine how the addition of interferograms with long temporal baselines impacts the PS solutions. In this test, 39 SAR images were combined to form 117 interferograms with 120-m spatial baseline as an upper limit but without any restriction on temporal baselines. In addition to the 86 combinations listed in Table I, 31 new interferograms with temporal baselines ranging from four to eight years are added. The solutions are carried out again with the new set of interferograms. Fig. 10 shows the histograms of the MC values of all the PS connections from this and the previous solutions. The addition of the 31 new interferograms actually reduces the number of good quality PS connections, for example, from 52% of the total number of PS connections to 46% when an MC threshold value of 0.45 is used. The number drops further from 40% to 28% if the MC threshold value is set as 0.5. The solution for the subsidence can still be carried out with the 117 interferograms, but the subsidence appears

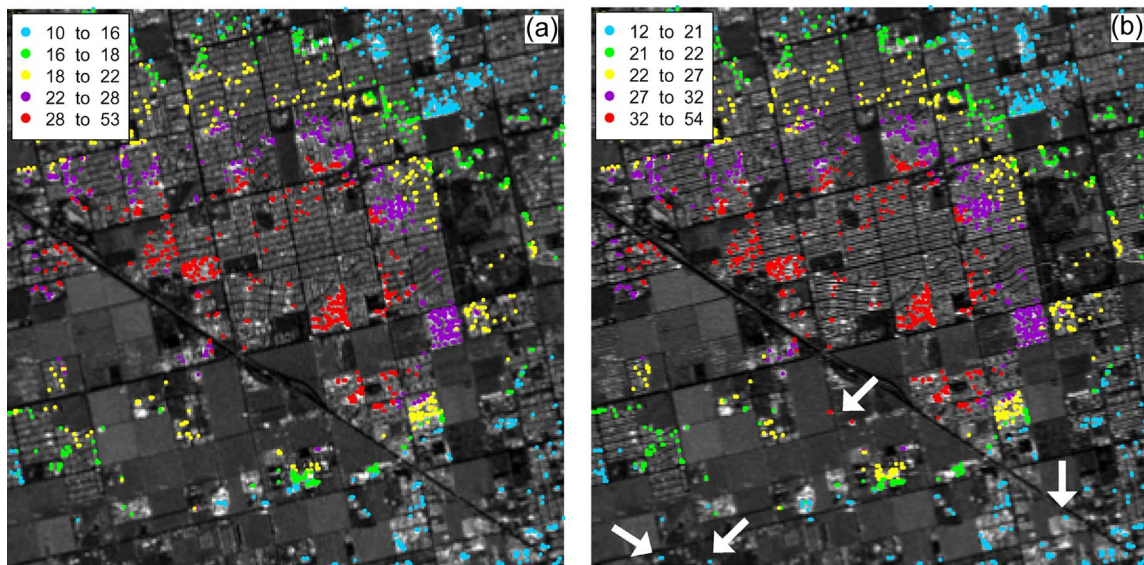


Fig. 8. PS points around Glendale and their subsidence rates (in millimeters per year) derived with (a) the TIN and (b) the FCN methods, respectively. The arrows indicate some of the PS points that remain in the FCN but not in the TIN.

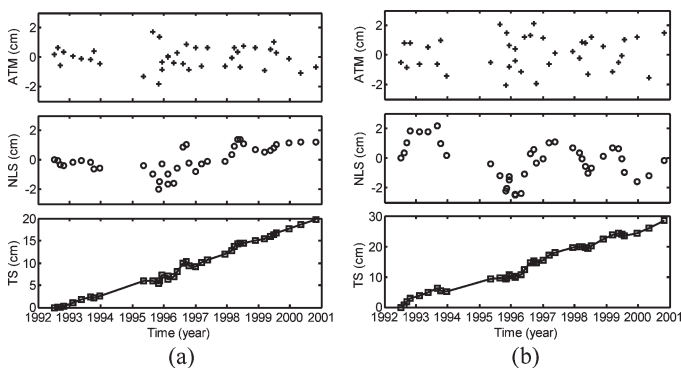


Fig. 9. Temporal variation of atmospheric (ATM) delays in the LOS direction, nonlinear subsidence (NLS), and total subsidence (TS) at two PS points as marked in Fig. 6. (a) is for P1 and (b) for P2.

underestimated in some localized areas due to the removal of some key PS connections and points. This indicates that the addition of interferograms with long temporal baselines may reduce the accuracy of the PS solutions. It should be noted that imposing a stricter restriction on temporal baselines (e.g., three years) can result in reduction in the redundancy and thus reduce the reliability of the PS solution. Therefore, the temporal-baseline threshold should be carefully selected to strike a balance between the accuracy and the reliability of the PS solution.

## VI. CONCLUSION

An improved PS-InSAR approach has been presented for the estimation of spatiotemporal surface displacements based on time series of SAR images. A strong PS network is formed by freely connecting a PS with all those within a given distance threshold, for example, 1 km. The increments of linear deformation rates and DEM errors along any connected PS pair are estimated from the multitemporal differential interferometric phase data by optimizing an objective function. An LS approach

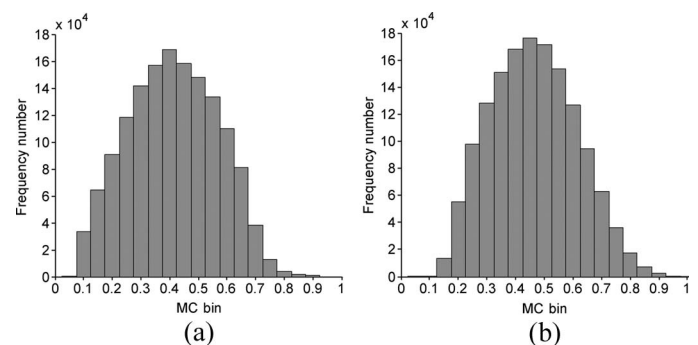


Fig. 10. Histograms of MC values computed for two data sets. (a) One hundred seventeen interferograms with temporal baselines up to eight years. (b) Eighty-six interferograms with temporal baselines shorter than four years.

is then applied to estimate the most probable linear deformation rates and DEM errors at all the PS points based on the increments along the PS pairs. Detecting and removing outlying increment values are an important part of the LS solutions. The nonlinear deformations and the atmospheric artifacts are finally determined based on the residual differential interferograms by successively applying the SVD and EMD methods.

An experiment has been carried out with the proposed method to detect the historical evolution of subsidence over western Phoenix, Arizona, with 39 ERS-1/2 C-band SAR images acquired during 1992–2000. The test results have shown two subsidence bowls with peak subsidence rates being 54 and 30 mm/yr, respectively, around the three towns in the area, Glenda, Peoria, and Sun City. The temporal variation of the nonlinear deformations falls within a dynamic range of several centimeters. The presented method has been able to recover the spatiotemporal ground deformations to a great extent, particularly over areas without clear interferometric fringes due to temporal decorrelation. For example, the deep subsidence bowl in Glendale can be completely delineated despite that no individual interferogram has shown full and clear fringes over this area.

Compared to the TIN, the FCN is much stronger and more advantageous in terms of both the accuracy and reliability measures, although the latter is computationally more demanding. The reliability of the FCN is enhanced due to the increase in the number of redundant observations (PS pairs). For example, in the test carried out, the number of PS pairs in the FCN is over 30 times more than that in the TIN, leading to a significant difference in the minimum redundancy number (0.96 versus 0.45). Most importantly, finer details of the deformations can be estimated with the FCN approach as it tends to keep more PS points in the network than the TIN approach, e.g., 14 428 PS points versus 12 250 for the experiment.

It has also been found that the temporal decorrelation still affects to certain extent the PS solutions. The addition of long temporal baseline interferograms may degrade the quality of the PS results.

As a final remark, it is emphasized that the exact separation of nonlinear deformations from atmospheric artifacts is a challenging task even with the EMD method proposed. Further improvement on this aspect is still required, for example, by integrating *a priori* information on atmosphere effects and/or deformations from GPS observations.

#### ACKNOWLEDGMENT

The authors would like to thank the U.S. Geological Survey for providing a seamless SRTM DEM of the study area and the Delft University of Technology for providing the precise orbital data. The authors would also like to thank P. Antonio for interesting discussions and D. Yang for assistance in SAR data processing.

#### REFERENCES

- [1] D. Massonnet and K. L. Feigl, "Radar interferometry and its application to changes in the Earth's surface," *Rev. Geophys.*, vol. 36, no. 4, pp. 441–500, 1998.
- [2] P. A. Rosen, S. Hensley, I. R. Joughin, F. K. Li, S. N. Madsen, E. Rodriguez, and R. M. Goldstein, "Synthetic aperture radar interferometry," *Proc. IEEE*, vol. 88, no. 3, pp. 333–382, Mar. 2000.
- [3] A. Ferretti, G. Savio, R. Barzaghi, A. Borghi, S. Musazzi, F. Novali, C. Prati, and F. Rocca, "Submillimeter accuracy of InSAR time Series: Experimental validation," *IEEE Trans. Geosci. Remote Sens.*, vol. 45, no. 5, pp. 1142–1153, May 2007.
- [4] S. Samsonov, K. Tiampo, J. Rundle, and Z. H. Li, "Application of DInSAR-GPS optimization for derivation of fine-scale surface motion maps of Southern California," *IEEE Trans. Geosci. Remote Sens.*, vol. 45, no. 2, pp. 512–521, Feb. 2007.
- [5] H. A. Zebker and J. Villaseñor, "Decorrelation in interferometric radar echoes," *IEEE Trans. Geosci. Remote Sens.*, vol. 30, no. 5, pp. 950–959, Sep. 1992.
- [6] R. F. Hanssen, T. M. Weckwerth, H. A. Zebker, and R. Klees, "High-resolution water vapor mapping from interferometric radar measurements," *Science*, vol. 283, no. 5406, pp. 1297–1299, Feb. 1999.
- [7] S. M. Buckley, P. A. Rosen, S. Hensley, and B. D. Tapley, "Land Subsidence in Houston, Texas, measured by radar interferometry and constrained by extensometers," *J. Geophys. Res.*, vol. 108, no. B11, pp. 2542–2554, 2003.
- [8] S. M. Buckley, *Radar Interferometry Measurement of Land Subsidence*. Austin, TX: Univ. Texas Austin, 2000.
- [9] G. X. Liu, X. J. Luo, Q. Chen, D. F. Huang, and X. L. Ding, "Detecting land subsidence in Shanghai by PS-networking SAR interferometry," *Sensors*, vol. 8, no. 8, pp. 4725–4741, Aug. 2008.
- [10] H. A. Zebker, P. A. Rosen, and S. Hensley, "Atmospheric effects in interferometric synthetic aperture radar surface deformation and topographic maps," *J. Geophys. Res.*, vol. 102, no. B4, pp. 7547–7563, 1997.
- [11] Z. W. Li, X. L. Ding, G. X. Liu, and C. Huang, "Atmospheric effects on InSAR measurements—A review," *Geomat. Res. Australas.*, no. 79, pp. 43–58, 2003.
- [12] G. X. Liu, X. L. Ding, Z. L. Li, Z. W. Li, Y. Q. Chen, and S. B. Yu, "Pre- and co-seismic ground deformations of the 1999 Chi-Chi, Taiwan earthquake, measured with SAR interferometry," *Comput. Geosci.*, vol. 30, no. 4, pp. 333–343, May 2004.
- [13] D. T. Sandwell and E. J. Price, "Phase gradient approach to stacking interferograms," *J. Geophys. Res.*, vol. 103, no. B12, pp. 30 183–30 204, 1998.
- [14] S. Lyons and D. Sandwell, "Fault creep along the southern San Andreas from InSAR, permanent scatterers, and stacking," *J. Geophys. Res.*, vol. 108, no. B1, pp. 2047–2070, 2003.
- [15] A. Ferretti, C. Prati, and F. Rocca, "Nonlinear subsidence rate estimation using permanent scatterers in differential SAR interferometry," *IEEE Trans. Geosci. Remote Sens.*, vol. 38, no. 5, pp. 2202–2212, Sep. 2000.
- [16] A. Ferretti, C. Prati, and F. Rocca, "Permanent scatterers in SAR interferometry," *IEEE Trans. Geosci. Remote Sens.*, vol. 39, no. 1, pp. 8–20, Jan. 2001.
- [17] B. M. Kampes and N. Adam, "Velocity field retrieval from long term coherent points in radar interferometric stacks," in *Proc. IEEE Int. Geosci. Remote Sens. Symp.*, 2003, vol. 2, pp. 941–944.
- [18] C. Colesanti, A. Ferretti, C. Prati, and F. Rocca, "Monitoring landslides and tectonic motions with the permanent scatterers technique," *Eng. Geol.*, vol. 68, no. 1/2, pp. 3–14, Feb. 2003.
- [19] P. Berardino, G. Fornaro, R. Lanari, and E. Sansosti, "A new algorithm for surface deformation monitoring based on small baseline differential SAR interferograms," *IEEE Trans. Geosci. Remote Sens.*, vol. 40, no. 11, pp. 2375–2383, Nov. 2002.
- [20] R. Lanari, O. Mora, M. Manunta, J. J. Mallorqui, P. Berardino, and E. Sansosti, "A small-baseline approach for investigating deformations on full-resolution differential SAR interferograms," *IEEE Trans. Geosci. Remote Sens.*, vol. 42, no. 7, pp. 1377–1386, Jul. 2004.
- [21] P. Lundgren, S. Usai, E. Sansosti, R. Lanari, M. Tesauero, G. Fornaro, and P. Berardino, "Modeling surface deformation observed with synthetic aperture radar interferometry at Campi Flegrei caldera," *J. Geophys. Res.*, vol. 106, no. B9, pp. 19 355–19 366, 2001.
- [22] S. Usai, "A least squares database approach for SAR interferometric data," *IEEE Trans. Geosci. Remote Sens.*, vol. 41, no. 4, pp. 753–760, Apr. 2003.
- [23] O. Mora, J. J. Mallorqui, and A. Broquetas, "Linear and nonlinear terrain deformation maps from a reduced set of interferometric SAR images," *IEEE Trans. Geosci. Remote Sens.*, vol. 41, no. 10, pp. 2243–2253, Oct. 2003.
- [24] P. R. Wolf and C. D. Ghilani, *Adjustment Computations: Statistics and Least Squares in Surveying and GIS*. New York: Wiley, 1997.
- [25] N. E. Huang, Z. Shen, S. R. Long, M. L. Wu, H. H. Shih, Q. Zheng, N. C. Yen, C. C. Tung, and H. H. Liu, "The empirical mode decomposition and Hilbert spectrum for nonlinear and nonstationary time series analysis," *Proc. R. Soc. Lond. A, Math. Phys. Sci.*, vol. 454, pp. 903–995, 1998.
- [26] T. A. Davis, *User Guide (Version 4.0)*, 2002. [Online]. Available: <http://www.cise.ufl.edu/research/sparse/umfpack>
- [27] R. A. Olea, *Geostatistics for Engineers and Earth Scientists*. Dordrecht, The Netherlands: Kluwer, 1999.
- [28] Z. W. Li, X. L. Ding, C. Huang, W. B. Zou, and Y. L. Chen, "Atmospheric effects on repeat-pass InSAR measurements over Shanghai region," *J. Atmos. Sol.-Terr. Phys.*, vol. 69, no. 12, pp. 1344–1356, Aug. 2007.
- [29] R. M. Goldstein and C. L. Werner, "Radar interferogram filtering for geophysical applications," *Geophys. Res. Lett.*, vol. 25, no. 21, pp. 4035–4038, 1998.
- [30] Z. W. Li, X. L. Ding, D. W. Zheng, and C. Huang, "Least squares based filter for remote sensing image noise reduction," *IEEE Trans. Geosci. Remote Sens.*, vol. 46, no. 7, pp. 2044–2049, Jul. 2008.
- [31] D. C. Ghiglia and M. D. Pritt, *Two-Dimensional Phase Unwrapping: Theory, Algorithms, and Software*. New York: Wiley, 1998.
- [32] P. Flandrin, G. Rilling, and P. Goncalves, "Empirical mode decomposition as a filter bank," *IEEE Signal Process. Lett.*, vol. 11, no. 2, pp. 112–114, Feb. 2004.
- [33] F. Casu, S. M. Buckley, M. Manzo, A. Pepe, and R. Lanari, "Large scale InSAR deformation time series: Phoenix and Houston case studies," in *Proc. IEEE Int. Geosci. Remote Sens. Symp.*, 2005, vol. 7, pp. 5240–5243.
- [34] W. F. Caspary, *Concepts of Network and Deformation Analysis*, J. M. Rüeger, Ed. Sydney, Australia: School Surveying, Univ. New South Wales, 1987.
- [35] X. L. Ding and R. Coleman, "Multiple outlier detection by evaluating redundancy contributions of observations," *J. Geod.*, vol. 70, no. 8, pp. 489–498, May 1996.





**Guoxiang Liu** received the B.Eng. degree in surveying engineering from the East China Institute of Geology, Fuzhou, China, in 1991, the M.Eng. degree in geomatics from the Southwest Jiaotong University, Chengdu, China, in 1994, and the Ph.D. degree in remote sensing from The Hong Kong Polytechnic University, Kowloon, Hong Kong, in 2003.

From September of 2005 to September of 2006, he was a Visiting Scholar and conducted research on synthetic aperture radar interferometry (InSAR) with Dr. Sean M. Buckley with the Department of Aerospace Engineering and Engineering Mechanics, The University of Texas at Austin. He is currently a Professor with the Department of Surveying Engineering, Southwest Jiaotong University. His current research interests are InSAR, radargrammetry, and digital photogrammetry for mapping regional topography and deformation.



**Sean M. Buckley** (M'96) received the B.S. degree in aeronautical and astronautical engineering from the University of Illinois at Urbana-Champaign, Urbana, in 1992 and the M.S. and Ph.D. degrees in aerospace engineering from The University of Texas at Austin, Austin, in 1994 and 2000, respectively.

From 2000 to 2004, he was a Research Engineer/Science Associate with the Center for Space Research, The University of Texas at Austin. Since 2004, he has been an Assistant Professor with the Department of Aerospace Engineering and Engineering Mechanics, The University of Texas at Austin. His current research interests are interferometric synthetic aperture radar algorithm development and deformation studies, and satellite and aircraft remote sensing.



**Xiaoli Ding** received the B.Eng. degree in surveying engineering from Central South University of Technology, Changsha, China, in 1983 and the Ph.D. degree from The University of Sydney, Sydney, N.S.W., Australia, in 1993.

From 1992 to 1996, he was a Senior Research Fellow/Lecturer/Senior Lecturer with Curtin University, Perth, WA, Australia. Since 1996, he has been an Assistant Professor/Associate Professor/Professor/Chair Professor with the Department of Land Surveying and Geo-Informatics, The Hong Kong Polytechnic University, Kowloon, Hong Kong. His current research interests are development of GPS and interferometric synthetic aperture radar algorithms, and studies of structural and ground deformations.



**Qiang Chen** received the B.Eng. degree in photogrammetry and remote sensing and the M.Eng. and Ph.D. degrees in geodesy from Southwest Jiaotong University, Chengdu, China, in 1997, 2000, and 2007, respectively.

Since 2004, he has been a Lecturer/Associate Professor with the Department of Surveying Engineering, Southwest Jiaotong University. From April of 2007 to April of 2008, he conducted a visiting research with Prof. Xiaoli Ding with the Department of Land Surveying and Geo-Informatics, The Hong Kong Polytechnic University, Kowloon, Hong Kong. His current research interests are topography and deformation mapping with interferometric synthetic aperture radar, photogrammetry, and remote sensing.



**Xiaojun Luo** received the B.Eng. and M.Eng. degrees in geology from the Chengdu University of Technology, Chengdu, China, in 1998 and 2003, respectively, and the Ph.D. degree in geodesy from Southwest Jiaotong University, Chengdu, in 2007.

He is currently a Lecturer with the Department of Surveying Engineering, Southwest Jiaotong University. His research interests are interferometric synthetic aperture radar and optical remote sensing.